Development of Molybdenum Phosphide Catalysts for Higher Alcohol Synthesis from Syngas by Exploiting Support and Promoter Effects

Iris C. ten Have, Eduardo Valle, Alessandro Gallo, Jonathan L. Snider, Melis S. Duyar, and Thomas F. Jaramillo**

Molybdenum phosphide (MoP) catalysts have recently attracted attention due to their robust methanol synthesis activity from CO/CO_2. Synthesis strategies are used to steer MoP selectivity toward higher alcohols by investigating the promotion effects of alkali (K) and CO-dissociating (Co, Ni) and non-CO-dissociating (Pd) metals. A systematic study with transmission electron microscopy, X-ray diffraction, X-ray photoelectron spectroscopy, and X-ray absorption spectroscopy (XAS) showed that critical parameters governing the activity of MoP catalysts are P/Mo ratio and K loading, both facilitating MoP formation. The kinetic studies of mesoporous silica-supported MoP catalysts show a twofold role of K, which also acts as an electronic promoter by increasing the total alcohol selectivity and chain length. Palladium (Pd) increases CO conversion, but decreases alcohol chain length. The use of mesoporous carbon (MC) support has the most significant effect on catalyst performance and yields a KMoP/MC catalyst that ranks among the state-of-the-art in terms of selectivity to higher alcohols.

1. Introduction

There is increasing interest in the production of alternative transportation fuels from nonpetroleum resources due to issues such as rising CO_2 emissions leading to climate change and the geographically constrained nature of fossil fuels.[1–3] The production of higher alcohols from syngas ($CO/CO_2/H_2$) is one possible route for incorporating more sustainable energy sources into the transportation sector, as higher alcohols have achieved widespread use as fuel blends to increase combustion efficiency and the octane number of gasoline.[4] Higher alcohols blended into US gasoline are currently produced from sugar fermentation, and increasing production can strain agricultural resources and land use. The catalytic transformation of syngas offers a more sustainable and potentially economical pathway for the synthesis of higher alcohols, as syngas can be produced from a variety of processes, including biomass gasification and CO_2 capture and hydrogenation. However, an industrial-scale process for the direct conversion of syngas to higher alcohols does not yet exist due to limitations of activity and selectivity of catalysts studied to date.[4] If a suitable catalyst can be developed for the synthesis of higher alcohols from syngas, this would enable the incorporation of carbon and hydrogen from a diverse set of resources into transportation fuels.

Higher alcohol synthesis (HAS) is a complicated catalytic process that involves many different reactions occurring simultaneously on the catalyst surface.[5] Regarding the mechanistic understanding, much can be learned from the methanol synthesis (MS) and the Fischer–Tropsch synthesis (FTS).[4,5] MS involves molecular CO adsorption,[6] whereas FTS requires CO dissociation, hydrogenation, and chain propagation.[7] HAS needs both molecular CO adsorption and chain propagation, which are complementary to each other and hence occur on different sites. Therefore, as suggested earlier by both theoretical and practical work,[8,9] HAS requires a dual site that facilitates bifunctional catalysis.[5]

Mo-based catalysts have attracted attention for syngas conversion due to their favorable selectivities toward oxygenated products.[3,4,10–19] Mo itself has relatively low activity for syngas conversion and yields primarily hydrocarbons. Consequently, most studies on Mo catalysts have focused on compounds in which Mo is bound to the ligands C, N, S, or P.[3,20] Mo_2C, Mo_2N, and MoS_2 show the activity for syngas conversion toward oxygenates, especially when doped with alkali metals such as potassium.[5] However, in most cases, selectivity toward hydrocarbons is inevitable, with methane being the main product.

I. C. ten Have, E. Valle, Dr. A. Gallo, Dr. J. L. Snider, Dr. M. S. Duyar, Prof. T. F. Jaramillo
Department of Chemical Engineering
Stanford University
Stanford, CA 94305-5025, USA
E-mail: melis@stanford.edu; jaramillo@stanford.edu

I. C. ten Have, E. Valle, Dr. A. Gallo, Dr. J. L. Snider, Dr. M. S. Duyar, Prof. T. F. Jaramillo
SUNCAT Center for Interface Science and Catalysis
SLAC National Accelerator Laboratory
Menlo Park, CA 94025, USA

I. C. ten Have
Inorganic Chemistry and Catalysis, Debye Institute for Nanomaterials Science
Utrecht University
Utrecht, The Netherlands

K/β-Mo_2C and K/γ-Mo_2N both suffer from high hydrocarbon selectivities.[10,21,22] MoS_2 catalysts need to be cofed with H_2S,[23] a poisonous and corrosive gas, to prevent deactivation during syngas conversion. Moreover, sulfur is incorporated in the products, which is in conflict with environmental legislation.[3,24] Recently, it was shown that silica-supported molybdenum phosphide (MoP) catalysts exhibit a high selectivity toward MS [25] from both CO and CO_2, and C_{2+} oxygenate formation from syngas has been reported over K-promoted MoP/SiO_2 catalysts.[3,11] However, investigations on the MoP system for HAS have only just begun, and it will be worthwhile to conduct wider screenings of promoters and supports and to better understand the structure and function of the catalytic centers.[4,20,25,26]

It is important to investigate support effects because they have a significant impact on the geometric and electronic properties of the active elements.[4,27] Particularly, when catalysts contain nano-sized metal particles, the support material is of the utmost importance for stability. Nano-sized metal particles have a high chemical potential and high surface free energy. These properties facilitate their catalytic activity. However, nanoparticles are also prone to sintering,[28] which leads to a decrease in available metallic surface area and therefore results in a lower catalytic activity. To prepare stable and active catalysts, metal nanoparticles should be dispersed across a suitable support material. Furthermore, the support material can affect the catalyst selectivity. Interactions between the support and the active elements can alter the electronic state of the active phase and thereby influence the selectivity. For example, it is reported in the literature that carbon nanotubes promote HAS for Mo-based catalysts.[15,16,29] The interaction of carbon π-electrons with chemical species is suggested to contribute to the catalytic behavior.[4]

Because the active phosphide phase is formed inside the support pores, the support morphology and nature play important roles in the synthesis of MoP catalysts. MoP catalysts reported previously for syngas conversion were synthesized using the temperature-programmed reduction (TPR) method ending at 600–700 °C and oxidic precursors of Mo and P.[11,14,25,30] This synthesis creates highly sintering conditions due to both the high-temperature requirement and the generation of a large quantity of water during the reduction of precursors.[22,31] To withstand these conditions, mesoporous supports can be used. These typically have high surface areas and facilitate confinement effects.[4,32] Thereby, they enable control over the MoP particle size and stabilize small MoP particles under these sintering synthesis conditions as well as during catalytic testing. The present study examines support effects on MoP by using a commercially available amorphous silica, a model silica with ordered mesopores (SBA-15), and a carbon-based analog of SBA-15, with a similar mesoporous structure. Silica has been studied extensively and remains the best-understood support system.[4]

Carbon supports draw our attention because they are reported to enhance C_{2+} oxygenate selectivity due to the metal-support interaction provided by their unique electronic structure.[4,15,16,32–34]

Because MoP demonstrates favorable selectivities toward oxygenated products, the use of promoters is investigated to direct the selectivity toward the desired higher alcohols. Alkali metals, particularly potassium, have been shown to promote HAS.[14] For MoS_2 catalysts, it was demonstrated that both the nature of the potassium precursor and the intimacy between potassium and MoS_2 play a crucial role in the formation of a selective HAS catalyst.[35] Additionally, it was discovered that potassium not only changes the electronic properties of the MoS_2 catalyst but also stabilizes alkoxy species, which contribute to the formation of higher alcohols via CO insertion.[23] Fischer–Tropsch metals, such as cobalt and nickel, are also common promoters for HAS catalysts with a high methanol selectivity.[13,18,19,21] Due to the high activity of silica-supported MoP catalysts for MS,[25] the present investigates the promotion of MoP catalysts with Fischer–Tropsch metals. Another strategy is promotion with Pd or Pt, which adsorb CO nondissociatively and promote CO hydrogenation to form oxygenated products.[36,37]

The present study optimizes and tunes the synthesis of supported MoP catalysts to increase their selectivity to higher alcohols by investigating the interactions between MoP and the support material as well as promoter effects. A systematic approach is used involving both commercial amorphous silica and a model silica support with an ordered pore structure and well-known nature. The role of the previously reported K promoter[11,14,23,25] is elucidated; Co, Ni, and Pd are screened as potential promoters; and carbon is explored as a promising support for HAS. In-depth knowledge is developed about the role of the MoP-support interactions and promoter effects, and a rational design strategy[38] is used to tune the product selectivity toward the desired C_{2+} products.[39] The present study shows that mesoporous carbon (MC) support unlocks HAS activity and designs a catalyst that ranks among the state-of-the-art Mo-based HAS catalysts reported to date.[4] This KMoP/MC catalyst demonstrates 5% CO conversion, 30% higher alcohol selectivity, and 2% higher alcohol yield at 270 °C, 6 MPa, and 30 h time on stream, which places it among the most selective Mo-based catalysts at a relatively low pressure of operation.[4] MoP is a promising catalyst for HAS, which can be further developed with the advancement of understanding about the active site under operating conditions and investigation of other support and promoters for the HAS reaction.

2. Results and Discussion

2.1. Optimization of Amorphous Silica-Supported MoP Catalysts

Before investigating promoter effects for HAS on MoP-based catalysts, a systematic study was first performed to understand the effect of synthesis parameters on the structure and activity of the KMoP on amorphous SiO_2 catalyst system developed previously for MS from CO and CO_2.[25] The key parameters for synthesis are identified in the following sections as the P/Mo ratio, K/Mo ratio, and MoP loading.

2.1.1. Increased Alcohol Selectivity with an Excess of Phosphorus

A parametric study of the P/Mo molar ratio shows that a 50% excess of phosphorus ($P/Mo = 1.5$) during catalyst synthesis leads to higher selectivity toward alcohols and lower selectivity toward CO_2 as compared to a stoichiometric amount of phosphorus ($P/Mo = 1.0$) and a 100% excess of phosphorus ($P/Mo = 2.0$), as shown in **Table 1**. A phosphorus loading in slight excess of the

Table 1. CO conversion (%) and product selectivities (%) for KMoP on SiO_2 with P/Mo = 1.0, 1.5, 2.0. The Mo weight loading and the K/Mo molar ratio are kept constant at 10% and 1.2, respectively. Reaction conditions: $T = 230\,°C$, $H_2/CO = 3$, and $P = 3$ MPa, at 8 h time on stream.

		Selectivity [%]				
Catalyst	^{X}CO	CH_3OH	$C_2{}^{+}OH$	CH_4	$C_2{}^{+}H_x$	CO_2
$KMoP/SiO_2$ (P/Mo = 1.0)	0.08	0	0	6.7	0	93.3
$KMoP/SiO_2$ (P/Mo = 1.5)	0.49	37.4	16.3	9.8	12.8	23.8
$KMoP/SiO_2$ (P/Mo = 2.0)	0.22	25.0	17.2	11.1	15.3	31.4

stoichiometric amount (P/Mo = 1.5) facilitates the formation of the active MoP phase because volatile phosphorus species can be lost during catalyst synthesis, as seen in the X-ray fluorescence (XRF) results (see Table S2A, Supporting Information). A loading too far from the stoichiometric amount (P/Mo = 2) can lead to lower activities due to phosphorus blocking the active sites for CO adsorption.[40]

This correlation between phase and activity is observed (Table 1) as the conversion increases from 0.08% to 0.49% when the P/Mo ratio increases from 1 to 1.5, respectively, and X-ray diffraction (XRD) characterization shows no discernable pattern for the former catalyst, while the latter displays prominent MoP peaks, as seen in **Figure 1**. An increase in the P/Mo ratio to 2.0 leads to a CO conversion decrease from 0.49% to 0.22% with P/Mo = 1.5 (see Table 1). The XRD pattern of the samples (see Figure 1) shows that a lower degree of crystallinity is obtained for the P/Mo = 2 catalyst. Based on insights obtained from XRF (extended discussion provided in the Supplementary Information) and XRD (Figure 1), it can be seen that excess phosphorus (nominal P/Mo = 2) results in some inhibition of the formation of a crystalline MoP phase. Further investigations focusing on in situ spectroscopy and XRD could shed more light on the effects of excess P during synthesis. Average crystallite size was calculated using the Scherrer equation. The average size for samples containing P/Mo = 1.5 and 2 was 14.3 and 11.4 nm, respectively, and no analysis could be performed on the stoichiometric (P/Mo = 1) sample due to the lack of peaks. These results suggest that an optimal excess of phosphorus is needed to form a crystalline MoP phase. Note that the Mo weight loading is 10% and the K/Mo molar ratio is 1.2 for all catalysts.

Amorphous silica-supported MoP samples with varying P/Mo ratios were further investigated using X-ray photoelectron spectroscopy (XPS) (see **Figure 2**). The spectra in the P 2p region show two distinct sets of doublets: The first around 128.3–128.9 eV and the second around 132.8–133.3 eV. The doublet at the lower binding energy is associated with phosphorus bonded to molybdenum in the form of a phosphide, and the doublet at the higher binding energy is generally assigned to oxidized phosphorus in the form of $PO_4{}^{3-}$.[41,42] The spectra in the Mo 3d region also show two different oxidation states. The lower binding energy region around 227.1–227.7 eV is assigned to MoP and the downfield region located at 231.9–232.1 eV to Mo^{6+} resulting from MoO_3 or interactions with a phosphate group. Both the phosphate and Mo^{6+} peaks are the prominent oxidation state for the P/Mo = 1.0 and P/Mo = 2.0 samples. However, in the sample with a 50% excess of phosphorus (P/Mo = 1.5), the peaks assigned to MoP in both the P 2p region (128.3–128.9 eV) and Mo 3d region (227.1–227.7 eV) dominate, thereby confirming stabilization of the MoP phase.

Table 2 shows the ratios of different species calculated from XPS data. There is a clear correlation between phosphate and Mo^{6+}; as one increases, so does the other. The table also clearly shows that there is an optimal P/Mo ratio to achieve the lowest ratio of oxidized species to MoP species. In all cases, the phosphate to phosphide ratio is larger than the $Mo^{6+}$to Mo^{3+}ratio due to the fact that all samples, except for the sample with P/Mo = 1, have an excess loading of phosphorus. Therefore, the excess

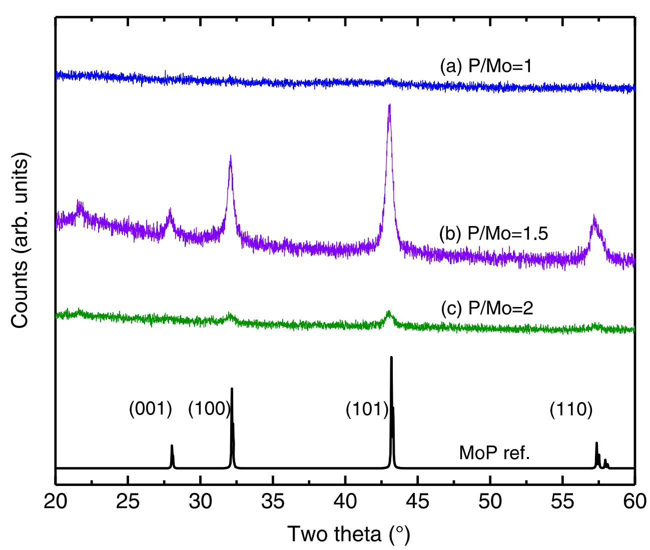

Figure 1. XRD patterns for passivated $KMoP/SiO_2$ samples with P/Mo ratios of a) 1.0, b) 1.5, and c) 2.0. The Mo weight loading and K/Mo molar ratio are kept constant at 10% and 1.2, respectively.

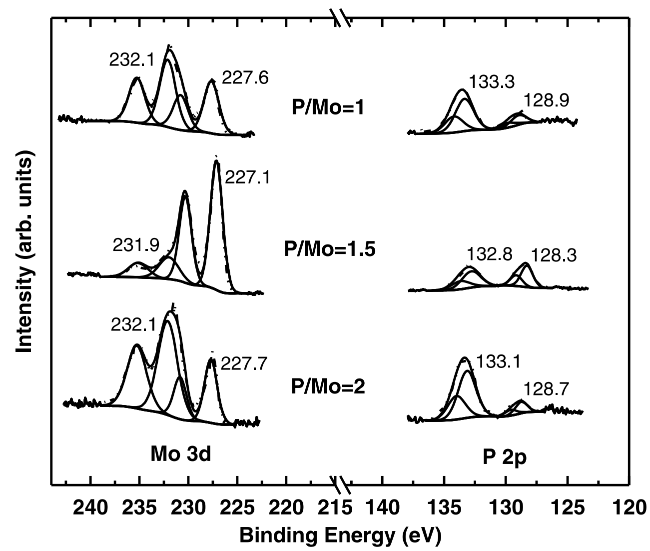

Figure 2. XPS spectra of Mo 3d (left) and P 2p (right) regions for the amorphous silica-supported samples with P/Mo = 1.0, 1.5, 2.0 from top to bottom. The Mo weight loading and K/Mo molar ratio are kept constant at 10% and 1.2, respectively.

Table 2. Molar ratios from XPS for KMoP on SiO_2 with P/Mo = 1.0, 1.5, 2.0. The Mo weight loading and the K/Mo molar ratio are kept constant at 10% and 1.2, respectively.

Catalyst	Phosphate/phosphide	Mo^{6+}/Mo^{3+}	P/Mo
$KMoP/SiO_2$ (P/Mo = 1.0)	4.00	1.39	1.92
$KMoP/SiO_2$ (P/Mo = 1.5)	1.19	0.27	1.35
$KMoP/SiO_2$ (P/Mo = 2.0)	6.25	2.27	1.79

phosphorus forms oxide species. A previous study using XPS showed that oxidized Mo species form on the surface of a silica-supported MoP catalyst upon exposure to air, and can be reduced using a pre-reduction treatment prior to catalytic testing.[25] The present study used the same pre-reduction treatment, which is expected to reduce the surface phosphate or the oxide of molybdenum prior to catalytic testing.

The use of P/Mo = 1.5 during synthesis leads to the stabilization of the MoP phase, which results in the most active catalyst (0.49% CO conversion). The formation of the fully phosphided MoP phase, through the use of excess P is critical for maximizing activity for CO hydrogenation and higher alcohol production, as evidenced by results shown in Table 1.

Methanol is the main product with 37.4% selectivity, followed by higher alcohols with 16.3%, in close agreement with prior work under similar operating conditions.[25] The catalyst prepared with P/Mo = 1.0 displays high levels of CO_2 production, with 93.3% selectivity, no alcohol production, and low activity (0.08% CO conversion). The methanation activity of this catalyst is attributed to the presence of a large amount of underphosphided Mo species on this catalyst formed during catalytic testing pre-reduction treatment, from oxidized Mo species (observed via ex situ XPS), in agreement with prior work.[25] CO_2 production can be indicative of water-gas shift activity.[3] A large excess of phosphorus (P/Mo = 2.0) results in a catalyst that retains favorable selectivity for higher alcohols (17.2%) yet displays a much lower CO conversion (0.22%) compared to the catalyst with P/Mo = 1.5, indicative of a poisoning effect. From these results, it can be seen that the higher alcohol yield is maximized for a phosphorus to molybdenum ratio of 1.5 (P/Mo = 1.5).

2.1.2. Increased Higher Alcohol Yield with 15 wt% Molybdenum

The TPR of oxidic precursors to yield MoP is known to be a hydrothermally sintering technique due to the release of water during the reduction of the precursors.[43] Hence, the effect of MoP loading on the catalyst properties such as particle size, phase formation, and activity can become significant due to water generation during synthesis, which can result in low catalytic surface area. The effect of loading on catalyst properties and activity was investigated by varying the Mo loading from 5 to 20 wt% while keeping a constant P/Mo ratio of 1.5 and constant K loading of 5%. Elemental analysis using XRF showed some discrepancies between the nominal loading of Mo and measured loadings (Table S2, Supporting Information), and this is attributed to the hygroscopic nature of the Mo precursor. However, as this leaves unchanged the monotonic increase in Mo loading achieved by increasing the amounts of Mo precursor and the conclusions drawn from the loading study, the catalysts are designated by their nominal loadings in the following discussion.

XRD patterns for these samples (see **Figure 3**) show prominent peaks corresponding to the bulk phase of MoP (see Figure S1, Supporting Information, and the corresponding section for XPS results), with different intensities corresponding to variations in crystallite size. Representative transmission electron microscopy (TEM) images of these catalysts are shown in **Figure 4**. Calculated crystallite sizes from XRD ($d_{101}{}^{XRD}$) and particle sizes from TEM ($d_{MoP}{}^{TEM}$) are presented in **Table 3** along with catalytic activity information pertaining to catalysts with varied Mo loadings. Although no discernible correlation exists between Mo loading and particle size in this range, conversion and higher alcohol yield are maximized for 15 wt% MoP, which can be attributed to the promotion effect of K. In the next section (Section 2.1.3), the effect of varying the K/Mo ratio on catalyst properties and activity is investigated.

2.1.3. Increased Higher Alcohol Selectivity with 5 wt% K

The effect of varying the K/Mo ratio on active phase formation and catalysis was investigated by synthesizing a series of $KMoP/SiO_2$ catalysts with fixed Mo loading (15 wt%) and P/Mo ratio (1.5). Elemental analysis of the K loading in each sample was performed using XRF, and the details are provided in the Supplementary Information (Table S2, Supporting Information). The XRD patterns in **Figure 5** show that in the absence of K, there are no MoP crystalline domains. As the K loading increases to 5 wt%, a very clear MoP pattern is observed. However, at 10 wt% K loading, the intensity in the pattern decreases. It is clear that there is an optimum level for K loading, which plays an important role in the formation of the MoP phase. Thus, in addition to any electronic promotion effects arising from the interaction of K and MoP, it is shown here that K also promotes the formation of the MoP phase during catalyst synthesis. This is presumably because K offers basic sites, which

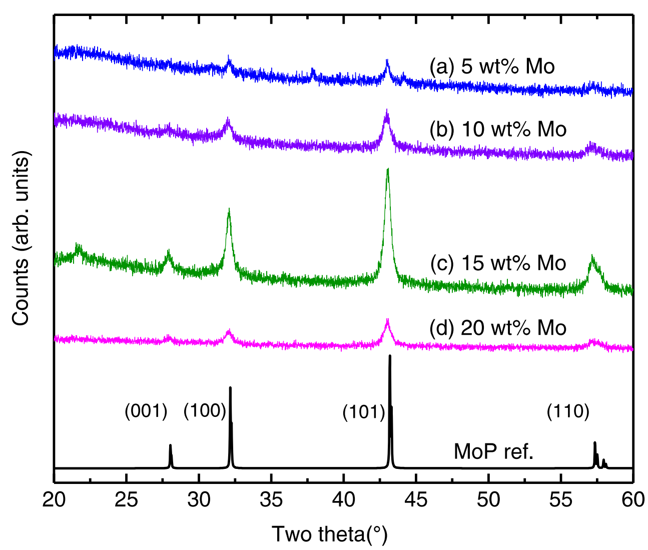

Figure 3. XRD patterns for passivated $KMoP/SiO_2$ samples with a) 5 wt% Mo, b) 10 wt% Mo c) 15 wt% Mo, and d) 20 wt% Mo.

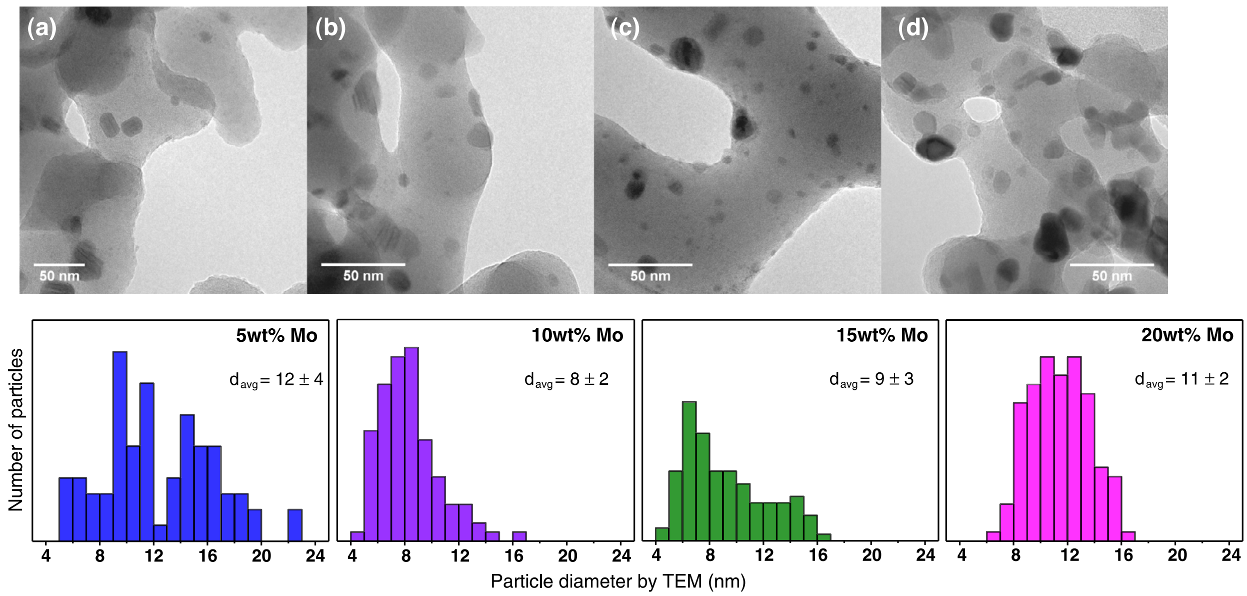

Figure 4. TEM images of KMoP/SiO_2 samples with a) 5 wt% Mo, b) 10 wt% Mo, c) 15 wt% Mo, and d) 20 wt% Mo.

Table 3. CO conversion (%), product selectivities (%), average particle sizes from TEM, and average crystallite sizes from XRD for KMoP on SiO_2 with 5, 10, 15, and 20 wt% Mo, while keeping a constant P/Mo ratio of 1.5 and a constant K loading of 5%. Reaction conditions: $T = 230\,°C$, $H_2/CO = 3$, and $P = 3$ MPa, at 14 h time on stream.

Catalyst	^{X}CO	Selectivity [%]					d_{MoP}*TEM*	d_{101}*XRD*
		CH_3OH	C_2^+OH	CH_4	$C_2^+H_x$	CO_2	[nm]	[nm]
KMoP/SiO_2 (5 wt% Mo)	0.24	25.2	16.1	8.5	12.6	37.5	12	22
KMoP/SiO_2 (10 wt% Mo)	0.26	33.3	20.9	12.3	16.6	16.8	8	13
KMoP/SiO_2 (15 wt% Mo)	0.49	37.4	16.3	9.8	12.8	23.8	9	18
KMoP/SiO_2 (20 wt% Mo)	0.11	16.0	6.6	9.7	9.4	58.3	11	16

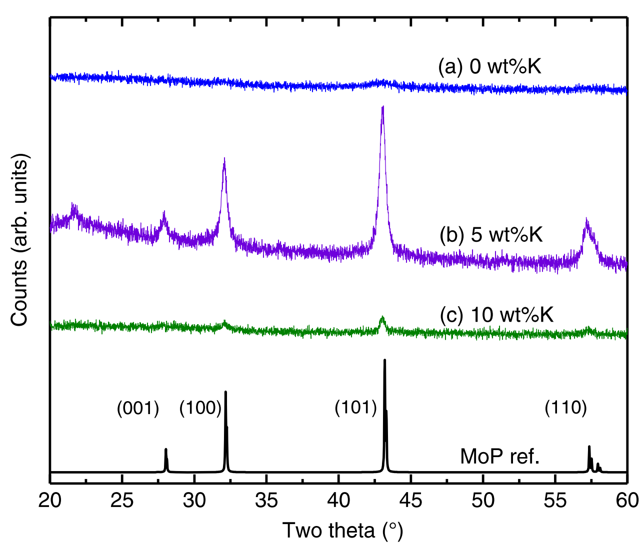

Figure 5. XRD patterns for passivated KMoP/SiO_2 samples with a) 0, b) 5, and c) 10 wt% K. The Mo wt% and P/Mo ratio are kept constant at 15 and 1.5, respectively.

facilitate a strong interaction with the anionic precursor complexes present during impregnation of the support (see also Section 1, Supporting Information), such as $[Mo_7O_{24}]^{6-}$, $[HPO_4]^{2-}$, and $[H_xP_2Mo_5O_{23}]^{(6-x)-}$.[44]

XPS results on MoP catalysts with varying K loading (see **Figure 6**) also confirm that K helps to facilitate interactions between Mo and P as seen from the binding energy shift to oxidation states corresponding to the MoP phase. The doublets in the P 2p region show that only the sample with 5 wt% K contains phosphorus in two different oxidation states, whereas the samples with 0 and 10 wt% K show phosphorus in one single oxidation state. The peak at 128.3 eV, which is attributed to phosphorus in MoP, is absent in the 0 and 10 wt% K samples; this is interpreted as a lower degree of phosphidation for Mo in these catalysts. The higher level of oxidation on the surface of the 0 and 10 wt% K samples is also evident in the Mo 3d region as the predominant doublets are found in the highly oxidized Mo^{6+} region,[45] between 231.8 and 232.3 eV. The predominant doublet in the 5 wt% K sample is found at 227.1 eV, which corresponds to molybdenum in MoP.

Table 4 shows the calculated ratios of phosphate/phosphide (from the P 2p region), Mo^{6+}/Mo^{3+} (from the Mo 3d region),

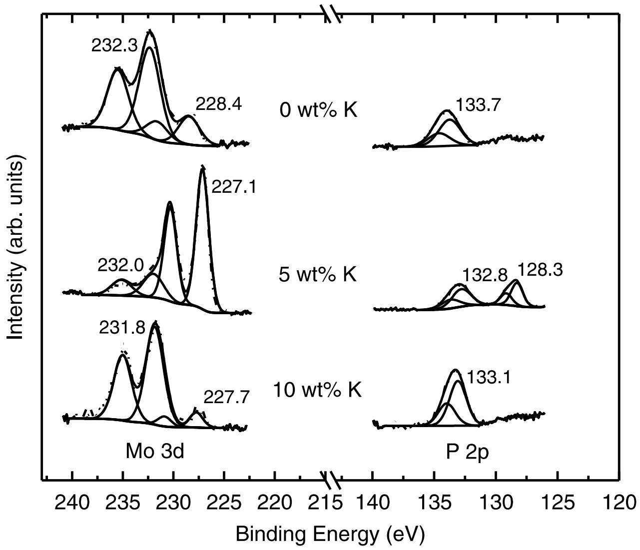

Figure 6. XPS spectra of Mo 3d (left) and P 2p (right) regions for the amorphous silica-supported samples with 0, 5, and 10 wt% K from top to bottom. The Mo wt% and P/Mo ratio are kept constant at 15 and 1.5, respectively.

Table 4. Molar ratios from XPS for KMoP on SiO_2 with 0, 5, and 10 wt% K. The Mo weight loading is kept constant at 15 wt%.

Catalyst	Phosphate/phosphide	Mo^{6+}/Mo^{3+}	P/Mo
KMoP/SiO_2 (0 wt% K)	N.D.	3.23	1.15
KMoP/SiO_2 (5 wt% K)	1.19	0.27	1.35
KMoP/SiO_2 (10 wt% K)	N.D.	9.09	1.94

and P/Mo. There is an optimal potassium loading to achieve the lowest ratio of oxidized species to MoP species. It was found previously that potassium is essential in producing the MoP crystal structure.[25] The potassium loading is vital to form the MoP phase both in bulk (see Figure 5) and on the surface. Adding no potassium leads to no phosphide species on the surface, whereas adding a large amount of potassium leads to a highly oxidized and P-rich surface. The increase in the P/Mo ratio as K increases could be indicative of the formation of phosphates of potassium.[42]

As shown in **Table 5**, the less oxidized sample, 5 wt% K, displays the highest total alcohol selectivity of 53% and 16.3% higher alcohol selectivity at 0.49% CO conversion. The sample with no K has the highest CO conversion of 0.61%, but only a 24% total alcohol selectivity, favoring methane, and longer chain hydrocarbons. The sample with 10 wt% K has a CO conversion of 0.21% and a CO_2 selectivity of 55%. As previously seen with the P loading study, the addition of some K boosts the higher alcohol yield; enhancement in higher alcohol yield is observed up to 5 wt% K loading. Loadings of K higher than 5 wt% adversely affect the higher alcohol yield. K is known to be an electronic promoter for HAS; the present study shows that on silica support, K is also critical for MoP formation during the high temperature (700 °C) catalyst synthesis process in accordance with our previous work.[25]

2.2. SBA-15-Supported K-Promoted MoP with Superior Activity

The previous sections show that the MoP phase formation is essential for high catalytic activity. The P/Mo ratio and K content play an essential role in the formation of the MoP phase. As mentioned previously, the MoP phase active for alcohol synthesis is formed under highly sintering conditions, resulting in low catalytic (MoP) surface areas. We move to the mesoporous SBA-15 system, which contains pores of uniform diameter (6.0 nm) in an attempt to stabilize MoP particles with controlled size distribution due to confinement effects. Following the systematic protocol outlined for amorphous silica-supported catalysts in Section 2.1, we performed an optimization of the K content (see Figure S2–S5, Supporting Information, and the corresponding discussion) and found the optimum K/Mo molar ratio to be 1.1 based on XRD (Figure S2, Supporting Information). MoP nanoparticles with average sizes of 5–6 nm were stabilized on the K/SBA-15 support as shown in Figure S3, Supporting Information. Additionally, we observed some Mo-rich regions on MoP/SBA-15 with TEM-energy-dispersive X-ray spectroscopy (EDS), although these regions were only a small portion of the analyzed sample (see Figure S4, Supporting Information, and the corresponding discussion).

2.3. Structure-Activity Relationships for K-MoP/SBA-15: Insights from XAS

After optimizing the K content as described in Section 2.2, we used XAS to obtain insights on the structure–activity relationships for K-MoP/SBA-15. As shown in **Table 6**, hydrocarbons are predominantly yielded (78.8% selectivity) on MoP/SBA-15

Table 5. CO conversion (%) and product selectivities (%) for KMoP on SiO_2 with 0, 5, and 10 wt% K. The Mo weight loading is kept constant at 15 wt%. Reaction conditions: $T = 230\,°C$, $H_2/CO = 3$, and $P = 3$ MPa, at 8 h time on stream.

		Selectivity [%]				
Catalyst	X_{CO}	CH_3OH	C_2^+OH	CH_4	$C_2^+H_x$	CO_2
KMoP/SiO_2 (0 wt% K)	0.61	17.9	5.7	21.8	37.3	13.0
KMoP/SiO_2 (5 wt% K)	0.49	37.4	16.3	9.8	12.8	23.8
KMoP/SiO_2 (10 wt% K)	0.21	20.2	8.2	6.7	10.4	54.6

Table 6. CO conversion (%) and product selectivities (%) for the SBA-15 supported MoP catalysts. The Mo weight loading is kept constant at 15%. Reaction conditions: $T = 270\,°C$, $H_2/CO = 2$, $P = 6$ MPa, and $GHSV = 2600\ h^{-1}$ at 30 h time on stream.

		Selectivity [%]				
Catalyst	X_{CO}	CH_3OH	C_2^+OH	CH_4	$C_2^+H_x$	CO_2
MoP/SBA-15	1.4	9.3	1.1	36.0	42.8	0.5
(0.5)-KMoP/SBA-15	1.7	28.9	17.7	25.8	26.1	1.1
(1.1)-KMoP/SBA-15	2.0	33.1	24.1	16.1	23.2	2.5

with a CO conversion of 1.4%. The total alcohol selectivity ($CH_3OH + C_{2+}OH$) is only 10.4%. Additionally, MoP/SBA-15 shows 9.2% selectivity to dimethyl ether (not shown in Table 6). Selectivity toward dimethyl ether was reported earlier in the literature for HAS catalysts and is generally assigned to the presence of acid sites.[12,46,47] Rational catalyst design suggests that the surface acidity, causing selectivity toward dimethyl ether and hydrocarbons, can be suppressed by alkali promotion. It was found that the addition of K as a promoter indeed increases the total alcohol selectivity to 46.6% and 57.2% for (0.5)-KMoP/SBA-15 and (1.1)-KMoP/SBA-15, respectively. Remarkably, the CO_2 selectivity remains below 2.5% for all catalysts. As discussed previously, the presence of K seems to assist in the formation of the MoP phase. Another possible role of K could be to act as a basic site during catalysis. Basic sites can stabilize formyl intermediates on the catalyst surface[23] so that C_2H_xO intermediates and subsequently higher alcohols can be formed.[19,35,46,48]

To thoroughly investigate the effect of K on the formation of the MoP phase, XAS data were collected both at the Mo K-edge (20 000 ev) and P K-edge (2140 eV). The Mo K-edge XAS data (**Figure 7**a) for SBA-15-supported catalysts clearly show how K plays a primary role in the formation of the MoP crystal phase during activation in hydrogen at 750 °C. The MoP phase does not form in the absence of K on SBA-15 (MoP/SBA-15). After calcination of the MoP precursors, an amorphous molybdenum phosphate ($MoPO_x$) is formed.[49] The edge position at 20 016 eV and the pre-edge feature at 20 006 eV show the presence of Mo^{6+} in distorted octahedral geometry surrounded by six O atoms.[50] The fit of the Fourier transform (FT) of the extended X-Ray absorption fine structure (EXAFS) oscillation (Figure 7b) indeed confirms the presence of six oxygen atoms bonded to Mo in a distorted octahedron.[51] No significant differences in both X-Ray absorption near edge structure (XANES) and EXAFS were shown for MoP/SBA-15 compared to $MoPO_x$. However, the EXAFS of (1.1)-KMoP/SBA-15 in Figure 7b shows two shells due to P and Mo atoms at a distance of 2.46 and 3.20 Å, respectively (see Table S8, Supporting Information), confirming the formation of MoP,[27,49] while a short-distance Mo—O shell highlights an incomplete reduction of the phosphate precursor. The presence of features in the 2140–2147 eV range of the P K-edge near edge X-ray absorption fine structure (NEXAFS) (Figure 7c) also confirms the formation of an appreciable amount of MoP for (1.1)-KMoP/SBA-15, while the phosphate peak at 2152.8 eV confirms the presence of $MoPO_x$.

There is a clear trend between the amount of K in the sample and the formation of MoP. K promotes the reduction of the amorphous phosphate precursor ($MoPO_x$) to MoP. However, a complete formation of MoP does not seem to be achieved even for higher K loading ((1.1)-KMoP/SBA-15). Alternatively, this could be ascribed to reoxidation of the surface layer after exposure to air. Noticeably, the progressive decrease in Mo—O coordination numbers and the increase in Mo—P shell with the increase in K loading (Table S8, Supporting Information) prove the beneficial effect of K for $MoPO_x$ reduction to MoP. The presence of a shell corresponding to P atoms surrounding Mo at a distance of 2.54 Å was identified for (0.5)-KMoP/SBA-15, while the unreduced Mo phosphate phase is still present, as evidenced by the significant Mo—O contribution. The longer Mo—P distance and a large Debye–Waller factor compared to that found for the Mo—P standard (2.44 Å) indicate incomplete phosphidation and hence the presence of amorphous MoP.[27,52] No evident shell corresponding to longer scattering path is consistent with an amorphous/well-dispersed morphology. An increase in K loading in (1.1)-KMoP/SBA-15 leads to a more defined Mo—P shell (Mo—P distance 2.44 Å) and the appearance of two different Mo scattering atoms in the second shell at a distance of 2.92 and 3.195 Å, respectively. The long Mo—Mo distance is consistent with the formation of MoP phase, whereas the short one is related to the presence of Mo-rich phosphide phases such as Mo_4P_3, Mo_8P_5, or Mo_3P because of an incomplete phosphidation process.[53] A small contribution due to oxidation, likely due to air exposure, is present. Comparison of the Mo K-edge XANES (Figure 7a) shows a progressive formation of phosphide as the pre-edge feature at 20 006 eV proper of $MoPO_x$ shifts toward higher energy and increases in intensity resembling more the

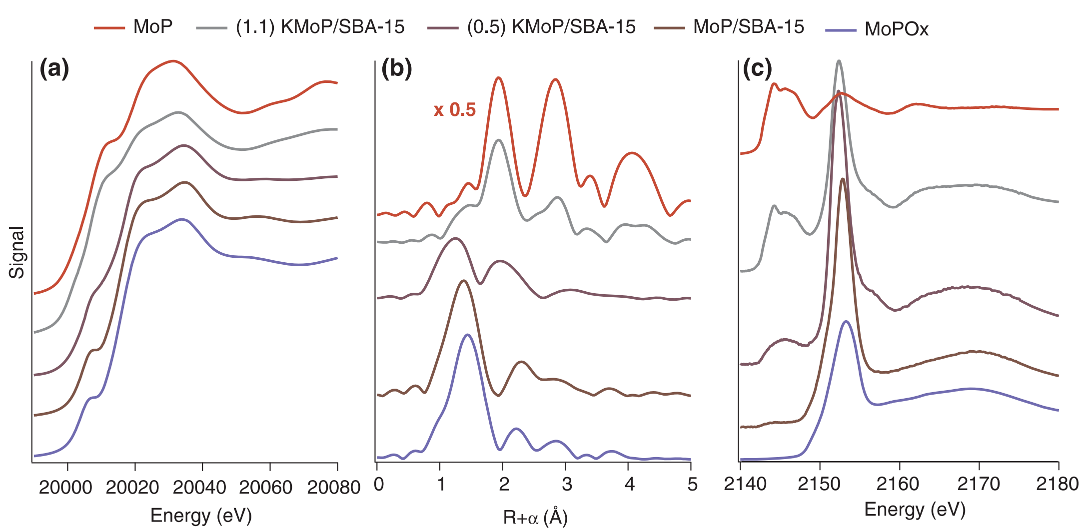

Figure 7. X-ray absorption spectra for SBA-15-supported samples, MoP standard, and $MoPO_x$ phosphate precursor. a) Mo K-edge XANES region; b) EXAFS; c) P K-edge NEXAFS region.

spectrum of MoP. A pronounced shoulder at the edge at 20 021 eV for all catalysts is indicative of oxidized Mo. P K-edge NEXAFS indicates that crystalline MoP is formed only for (1.1)-KMoP/SBA-15 (Figure 7b). The phosphate peak shifts toward 2152.3 eV and shows a different shape than in $MoPO_x$ for K-promoted catalysts, thus indicating the formation of a different phosphate after activation/air exposure.

2.4. Effect of Operating Conditions for HAS from Syngas

After optimizing synthesis parameters to maximize catalytic (MoP) surface area, the degree of phosphidation, and intimate contact with K promoter, the catalytic testing conditions are optimized, namely targeting the H_2/CO ratio and temperature favoring HAS over C1 products and hydrocarbons.

Figure 8a shows the product selectivities and CO conversion with respect to the H_2/CO ratio for (1.1)-KMoP/SBA-15 (5 wt% Mo). $H_2/CO = 3$ favors the formation of methanol and methane, which is in accordance with kinetic analyses reported in the literature for K/MoS_2.[54] Following the decrease of H_2/CO to 2 or 1, the formation of higher alcohols and higher hydrocarbons is favored. At $H_2/CO = 2$, the CO conversion is about twice as high compared to that when $H_2/CO = 1$. Consequently, the total higher alcohol yield exhibits a maximum at $H_2/CO = 2$.

Figure 8b shows the product selectivities and CO conversion with respect to the temperature for (1.1)-KMoP/SBA-15 (15 wt% Mo). The CO conversion increases linearly with temperature. From 230 to 270 °C, the total alcohol selectivity increases, whereas the total hydrocarbon selectivity decreases. At temperatures above 270 °C, the total alcohol selectivity decreases again, whereas the total hydrocarbon selectivity increases. Consequently, the total higher alcohol formation exhibits a maximum at 270 °C. The CO_2 selectivity is not plotted in Figure 8 because it is below 3% in all cases.

2.5. Kinetic Enhancement Due to K: Mechanistic Insights from Anderson–Schulz–Flory Distributions

Anderson–Schulz–Flory (ASF) plots can provide mechanistic insights, and hence, this analysis was performed to gain information on the kinetics and explain the enhanced catalytic performance in the presence of K. The ASF plots for alcohols and hydrocarbons at 30 h time on stream are shown in **Figure 9**. Linear ASF distributions are observed for alcohols and hydrocarbons over the entire C_n range for each catalyst. The observation of the correlated α values is in agreement with a common mechanism of alcohol formation by CO insertion into the same type of intermediate for hydrocarbon formation.[55] The α value for

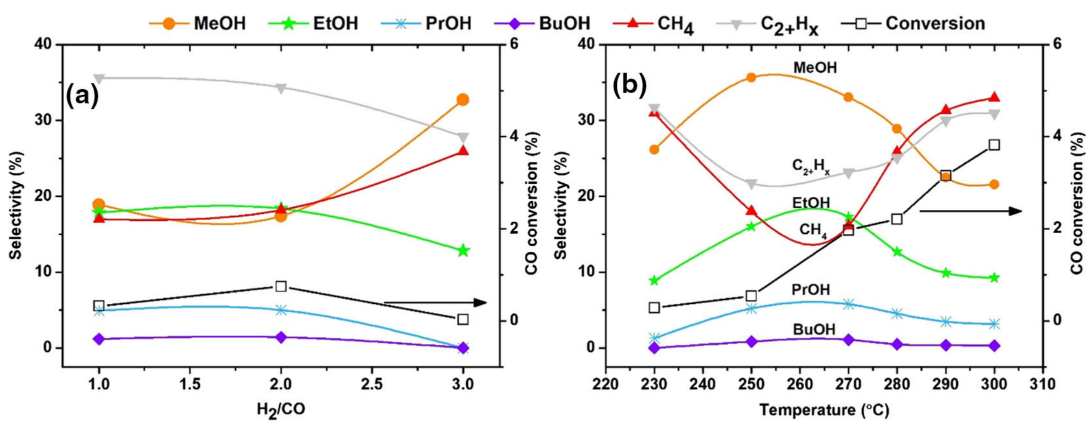

Figure 8. Product selectivities and CO conversion (black) at $P = 6$ MPa and GHSV = 2600 h^{-1} for a) (1.1)-KMoP/SBA-15 (5 wt% Mo) as a function of H_2/CO at $T = 270$ °C and b) (1.1)-KMoP/SBA-15 (15 wt% Mo) as a function of temperature at $H_2/CO = 2$.

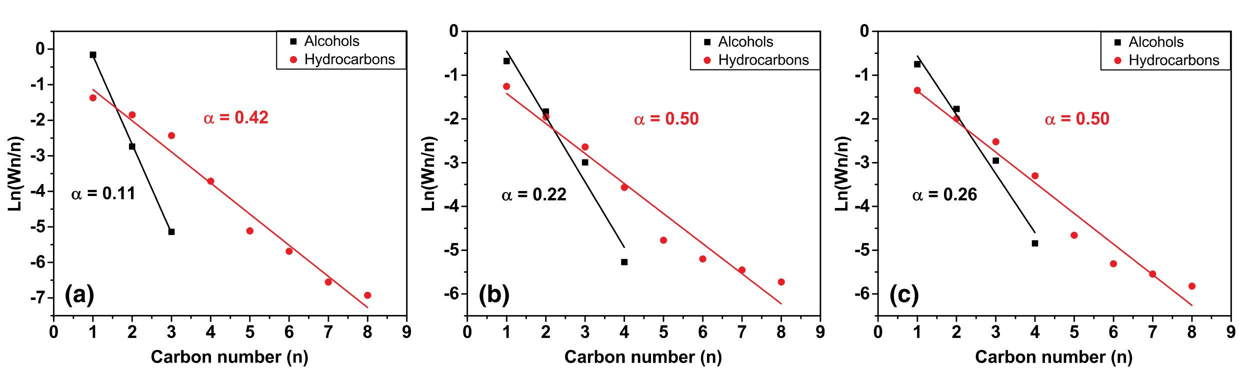

Figure 9. ASF plots for a) MoP/SBA-15, b) (0.5)-KMoP/SBA-15, c) (1.1)-KMoP/SBA-15 calculated at 30 h TOS.

alcohol formation increases upon the addition of K to the catalyst from 0.11 to 0.22 at K/Mo = 0.5 and 0.26 at K/Mo = 1.1. This indicates that alcohol products with longer chain length are formed, which is supported by a higher C_2^+OH selectivity (see Table 6). The addition of alkali promoters has been reported to increase α.[3] More mechanistic insights were obtained by calculating the apparent activation energies for CO conversion and the formation of methane and alcohols from Arrhenius plots (see Figure S9 and Table S6, Supporting Information). An elaborate discussion on the activation energies can be found in Section 5, Supporting Information. The results suggest indeed an increasing alcohol chain length upon the addition of K and alcohol chain growth via a CO insertion mechanism.

2.6. Promoters: Ni, Co, and Pd

Ni (5 wt%) and Co (3 wt%) were investigated as Fischer–Tropsch active metal promoters, and Pd (5 wt%) was investigated as a promoter due to its ability to adsorb CO nondissociatively and promote CO hydrogenation to form oxygenated products.[36,37] Elemental analysis was performed on as-synthesized catalysts using XRF, and the results show reasonable agreement with the nominal values (Table S5, Supporting Information). From the XRD patterns in **Figure 10**, the MoP phase is clearly observed for all promoted catalysts. Additionally, the promoted catalysts display peaks associated with NiO, CoO, and/or Co_3O_4, and $Pd_{15}P_2$ (see Supporting Information for detailed discussion and reference spectra). The catalytic performances of the promoted catalysts are shown in **Table 7**. Ni-(1.1)-KMoP/SBA-15 only converts 0.2% CO with methanol as the main product. Co-(1.1)-KMoP/SBA-15 only converts 0.02% CO with hydrocarbons as the main product. In the present study, both Ni and Co seem to poison the catalyst, rather than promoting HAS. However, it may be worthwhile to investigate different synthesis methods and promoter weight loadings while using probe molecule studies (such as CO chemisorption-infrared (IR) spectroscopy, temperature-programmed desorption) to inform the future development of metal-promoted MoP and ternary phosphide catalysts for HAS. Upon the addition of Pd to the

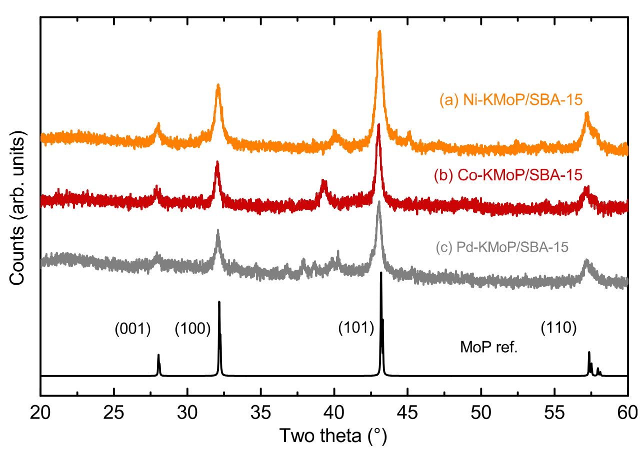

Figure 10. XRD patterns for passivated samples. a) Ni-KMoP/SBA-15. b) Co-KMoP/SBA-15. c) Pd-KMoP/SBA-15. All catalysts contain 15 wt% Mo. The Ni, Co, and Pd weight loadings are 5%, 3%, and 5%, respectively.

Table 7. CO conversion (%) and product selectivities (%) for the promoted catalysts. The Mo weight loading is kept constant at 15%. The Ni, Co, and Pd weight loadings are 5%, 3%, and 5%, respectively. Reaction conditions: $T = 270\,°C$, $H_2/CO = 2$, $P = 6$ MPa, and GHSV = 2600 h^{-1} at 30 h time on stream.

		Selectivity [%]				
Catalyst	^{X}CO	CH_3OH	C_2^+OH	CH_4	$C_2^+H_x$	CO_2
Ni-(1.1)-KMoP/SBA-15	0.20	59.0	5.7	20.0	10.9	0.5
Co-(1.1)-KMoP/SBA-15	0.02	30.8	0.0	27.3	42.0	0.0
Pd-(1.1)-KMoP/SBA-15	4.9	36.8	17.0	20.7	23.2	0.9

(1.1)-KMoP/SBA-15 catalyst, the CO conversion increases from 2.0% to 4.9%. However, methanol is the main product and the C_2^+OH selectivity decreases from 24.1% to 17.0%. A linear ASF distribution is observed for this catalyst with $\alpha = 0.21$ and 0.55 for alcohols and hydrocarbons, respectively (see Figure S6A, Supporting Information). The apparent activation energy (see Table S6, Supporting Information) also increases with increasing alcohol chain length. The overall effect of the Pd promoter seems beneficial for HAS because the total higher alcohol yield increases from 0.5% to 0.8%.

2.7. MC Support Improves HAS Activity

2.7.1. Kinetics and Catalysis

Carbon supports have shown promising results for HAS, as reported in the literature.[15,32,56] The graphitic carbon structure plays an important role in CO hydrogenation; the electron conductivity of graphitic carbon structures can facilitate electron transfer between metal species and CO molecules, which activates the CO molecules.[15,32] To investigate this effect, an MC analog of SBA-15 (Starbon 800) was chosen, which is referred to as MC in the following discussion.

Figure 11 shows that the MoP phase is exclusively formed on K/MC. (1.1)-KMoP/MC shows enhanced catalytic performance compared to all other catalysts in this study, with a steady-state CO conversion of 5.0% and a total alcohol selectivity of 58.0% at

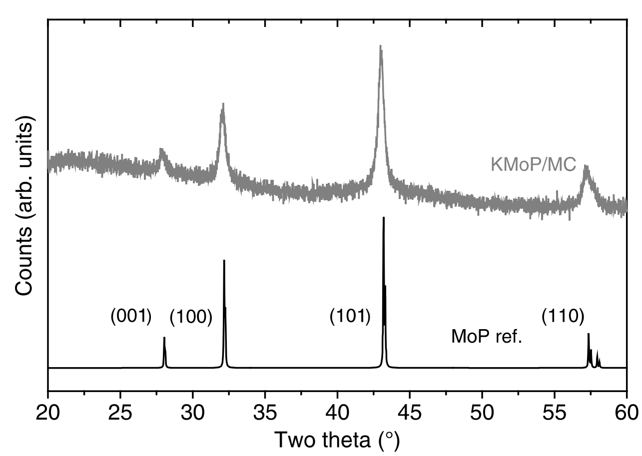

Figure 11. XRD pattern for passivated (1.1)-KMoP/MC.

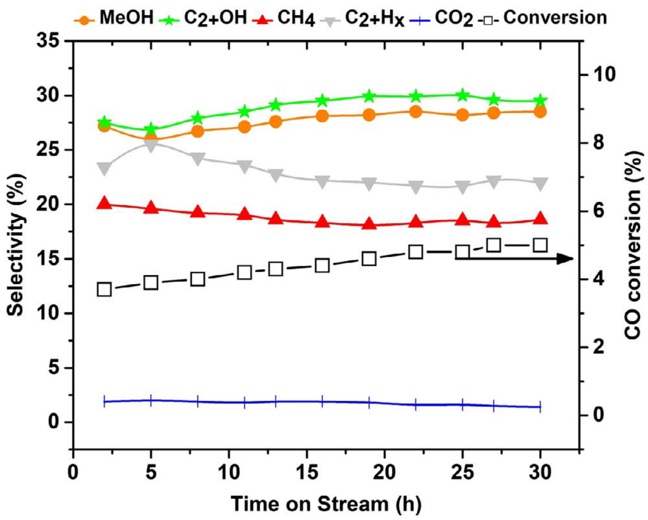

Figure 12. Product selectivities and CO conversion (black) as a function of time on stream for (1.1)-KMoP/MC (15 wt% Mo) at $T = 270\,^{\circ}C$, $H_2/CO = 2$, $P = 6$ MPa, and GHSV $= 2600\,h^{-1}$.

30 h time on stream (see **Figure 12** and **Table 8**). Higher alcohols ($C_2^{+}OH$) are the main products for CO conversion over (1.1)-KMoP/MC with a yield (Y_{HA}) of 1.5%, which ranks this catalyst among the state-of-the-art Mo-based HAS catalysts.[4] Remarkably, ethanol forms the largest weight fraction in the total alcohol products (wt% of ethanol in the total alcohols), followed by methanol, propanol, butanol, and pentanol (see Table S7, Supporting Information). A linear ASF distribution is observed for this catalyst with $\alpha = 0.43$ and 0.55 for alcohols and hydrocarbons, respectively (see Figure S6B, Supporting Information). The apparent activation energy (see Table S6, Supporting Information) decreases with increasing alcohol chain length, suggesting that the formation of formyl surface species might form a bottleneck in HAS over (1.1)-KMoP/MC.

Figure 12 shows the excellent stability of (1.1)-KMoP/MC over 30 h time on stream. Both the CO conversion and the total alcohol selectivity increase over time, whereas the hydrocarbon selectivity decreases. Increases in CO conversion and total alcohol selectivity are observed for all K-promoted catalysts in this study. This phenomenon is likely caused by potassium spreading over the catalyst surface during reaction,[35] which results in more intimate contact between K and MoP and thereby improves catalyst performance. It should be noted that potassium plays an essential role in the formation of the MoP phase (see Section 2.1.3 and 2.2) and thereby improves HAS. A MoP/MC catalyst was also tested in this study as a control. This catalyst displayed a CO conversion of 0.8% with selectivity mainly toward CO_2 and hydrocarbons (see Figure S10, Supporting Information), which highlights the electronic promotion effect of K in addition to structural promotion during MoP phase formation.

Table 8. CO conversion (%) and product selectivities (%) for the three best catalysts in this study. The Mo weight loading is kept constant at 15% and the Pd loading is 5 wt%. Reaction conditions: $T = 270\,^{\circ}C$, $H_2/CO = 2$, $P = 6$ MPa, and GHSV $= 2600\,h^{-1}$ at 30 h time on stream.

		Selectivity [%]				
Catalyst	^{X}CO	CH_3OH	$C_2^{+}OH$	CH_4	$C_2^{+}H_x$	CO_2
(1.1)-KMoP/SBA-15	2.0	33.1	24.1	16.1	23.2	2.5
Pd-(1.1)-KMoP/SBA-15	4.9	36.8	17.0	20.7	23.2	0.9
(1.1)-KMoP/MC	5.0	28.5	29.5	18.6	22.0	1.4

2.7.2. Formation of the MoP Phase Investigated with XAS

To investigate the effect of K on the formation of the MoP phase on MC-supported catalysts XAS data were collected at both the Mo K-edge (20 000 ev) and P K-edge (2140 eV). The comparison of the Mo K-edge XAS data (see **Figure 13**a) indicates that K plays a role in the formation of the MoP crystal phase during activation in hydrogen at 750 °C; this is, however, less pronounced than that for the SBA-15-supported catalysts (see Figure 7a). The MoP phase is partially formed on MC without K (MoP/MC), along with an amorphous molybdenum phosphate ($MoPO_x$).[49] The edge position at 20 016 eV and the pre-edge feature at 20 006 eV show the presence of Mo^{6+} in distorted octahedral geometry surrounded by six O atoms.[50] The fit of the FT of the EXAFS oscillation indeed confirms the presence of six oxygen atoms bonded to Mo in a distorted octahedron.[51] For MoP/MC, the pre-edge feature in XANES (see Figure 13a) shifts toward higher energy and significantly grows in intensity compared to $MoPO_x$. Besides, the EXAFS of MoP/MC (see Figure 13b) shows two shells due to P and Mo atoms at a distance of 2.44 and 3.20 Å, respectively (Table S9, Supporting Information), confirming the formation of MoP,[27,49] whereas a short-distance Mo—O shell highlights an incomplete reduction of the phosphate precursor. The presence of features in the 2140–2147 eV range ascribable to MoP in the P K-edge NEXAFS (see Figure 13c) also confirms the formation of an appreciable amount of MoP for MoP/MC, along with a phosphate peak at 2152.8 eV similar to $MoPO_x$. Even upon the addition of K, the complete formation of MoP does not seem to be achieved, which could also be ascribed to reoxidation of the surface layer after exposure to air. Noticeably, the decrease in Mo—O coordination numbers and the increase in Mo—P shell in the presence of K (Table S9, Supporting Information) prove the beneficial effect of K for $MoPO_x$ reduction to MoP. The presence of a shell corresponding to P atoms surrounding Mo at a distance of 2.44 Å was identified for all MC-supported catalysts, while the unreduced Mo phosphate phase is still present, as evidenced by the significant Mo—O contribution.

2.7.3. MoP Phase Remains Present on MC after Catalysis

To investigate the stability of (1.1)-KMoP/MC, XAS data before and after catalysis were compared. The small shell due to oxidized Mo for (1.1)-KMoP/MC post-reaction and (1.1)-KMoP/MC pre-reaction is likely related to air exposure of the catalysts. The Mo K-edge XANES of (1.1)-KMoP/MC (see Figure 13a) both before and after the catalytic testing closely resembles the one of MoP. Small differences due to nanoparticle dispersion and oxidation are present. The presence of a clear shell at higher (non-phase-corrected) distances (3.5–4.5 Å) mainly related to a longer Mo–Mo scattering path indicates the presence of large well-crystallized nanoparticles for the supported catalysts. The

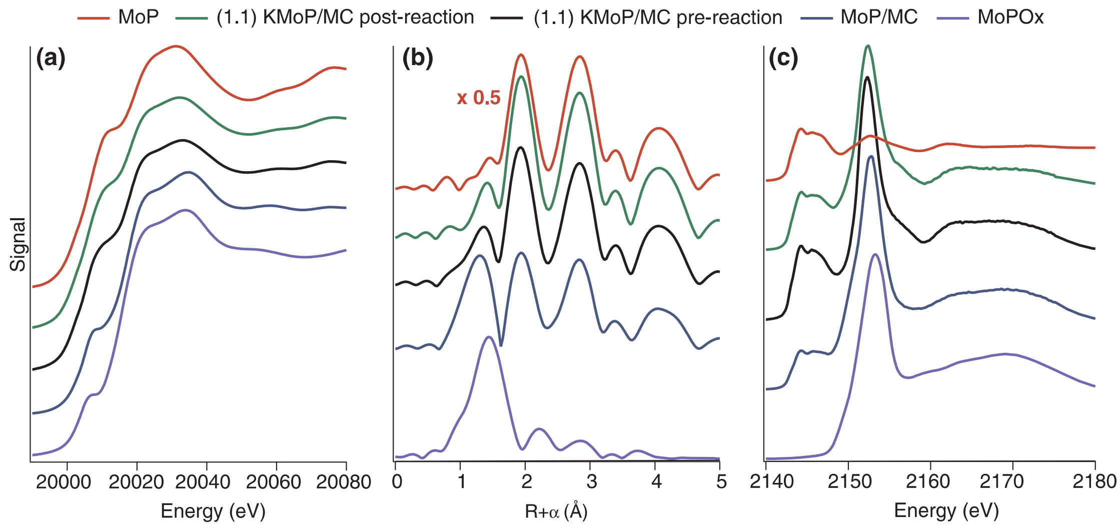

Figure 13. X-ray absorption spectra for MC-supported samples, MoP standard, and $MoPO_x$ phosphate precursor. a) Mo K-edge XANES region. b) EXAFS. c) P K-edge NEXAFS region.

coordination numbers for (1.1)-KMoP/MC post-reaction for Mo–P and Mo–Mo increase slightly after catalytic testing (see Table S9, Supporting Information), indicating some sintering during catalysis, which does not seem to affect the performance of this catalyst over 30 h time on stream (see Figure 12). XANES spectra at the Mo K-edge (see Figure 13a) and NEXAFS at the P K-edge (see Figure 13c) confirm the formation of well-crystallized MoP in the presence of K and a phosphate peak at 2152.3 eV, analogous to the one for K-promoted SBA-15-supported catalysts, is present. In general, lower coordination numbers for Mo–P and Mo–Mo were obtained for the supported catalysts than for bulk MoP, indicating the presence of supported MoP nanoparticles.

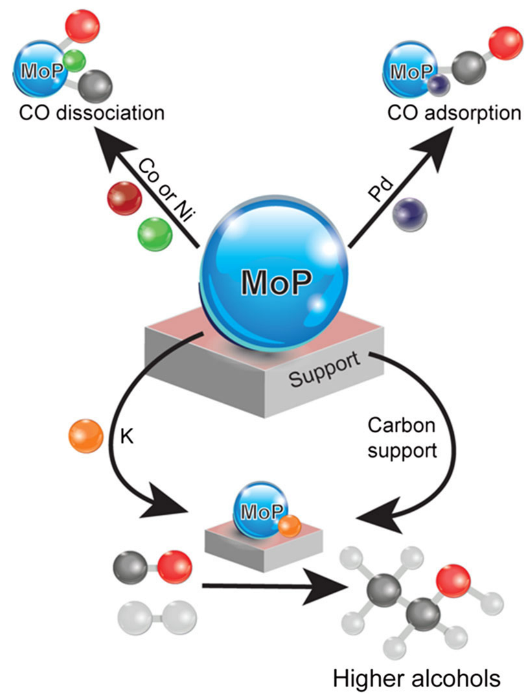

Figure 14. Summary of strategies explored to promote HAS activity of MoP catalysts.

3. Conclusions

In summary, the present study optimized and tuned the synthesis of supported MoP catalysts to increase their selectivity to higher alcohols by investigating the support morphology, support nature, and promoter effects (see **Figure 14**). Both an excess of P and the presence of K during the catalyst synthesis facilitate the formation of the catalytically active MoP phase on amorphous silica support. K possibly acts as a basic site and stabilizes formyl intermediates during catalysis. Moreover, the catalytic performance was improved with a mesoporous silica (SBA-15) support, which stabilized nanosized MoP particles with controlled size distribution and confinement effects. With this system, the catalytic testing conditions were optimized to favor HAS over C1 products and hydrocarbons. Co and Ni seemed to act as poisons rather than promoters, while the Pd promoter increased CO conversion, but produced alcohol products with lower chain length. Changing the support nature by using a carbon analog of the mesoporous silica enabled to increase the CO conversion to 5.0% and the total alcohol selectivity to 58.0%, with higher alcohols (C_2^+OH) as the main products. This catalytic performance ranks the developed carbon-supported catalyst ((1.1)-KMoP/MC) among the state-of-the-art Mo-based HAS catalysts. The results highlight the importance of conducting a systematic study looking at the catalyst system as a whole and exploring support and promoter effects on both synthesis and catalytic performance. The use of microscopy, diffraction, and X-ray spectroscopy techniques allows to identify both the structural and electronic promotion effects arising from the use of various supports and promoters. Supported MoP catalysts are promising catalysts for HAS, and by further exploring a rational design strategy, they have great potential in future applications.

4. Experimental Section

Support Materials and Synthesis: Commercial SiO_2 (Perkasil SM 660, Grace Davison) was used as an amorphous support material. Catalysts were prepared with washed and unwashed SiO_2. The washing step served to remove any sodium impurities that might remain from the sodium silicate synthesis precursor.[57] Silica was washed in 2 M nitric acid for 2 h at 80 °C. The washed silica was then rinsed with deionized water to remove nitric acid followed by drying at 120 °C overnight. Hexagonally ordered mesoporous silica (SBA-15) was synthesized by dissolving 24.1 g triblock copolymer P123 in a solution of 400 g deionized water and 12.7 g HCl (37%) in a 1000 mL polypropylene bottle. The resulting solution was left to dissolve P123 overnight at 40 °C under magnetic stirring. Then, 47.4 g of TEOS was added, and the solution was left under magnetic stirring for 24 h. Subsequently, the white suspension was hydrothermally treated at 100 °C for 48 h in a Teflon-lined autoclave. After cooling to room temperature, the solid product was recovered by washing with a 1500 mL deionized water/ethanol solution (1:1 by volume) and static drying at 120 °C. The compound was calcined in a muffle furnace at 550 °C for 6 h with a heating rate of 4.4 °C min^{-1} to remove the remaining structure-directing agent.

MC (Starbon 800) was purchased from Sigma—Aldrich and used as a support material without any further treatment.

Support Characterization: Textural Properties: Nitrogen physisorption was used to characterize the textural properties of the support materials. Nitrogen physisorption isotherms were measured at −196 °C on a Micromeritics 3-Flex instrument. Before the measurements, samples were dried at 250 °C under vacuum below 0.5 torr for 12 h. Specific surface areas were calculated using the multipoint Brunauer–Emmett–Teller (BET) method ($0.05 < p/p_0 < 0.25$). Furthermore, the pore volumes (V_{pore}), pore size distributions, and average pore diameters were determined by the Brunauer–Joyner–Halenda (BJH) method by using the desorption branches of the isotherms. The results and corresponding discussion can be found in the supplementary information (Section 1, Supporting Information).

Point of Zero Charge: The point of zero charge for all supports was measured by applying the mass titration method. Suspensions of 10 and 20 wt% support material in 0.1 M NaCl were prepared and stirred magnetically. The pH values of the suspensions were measured after 24 h of contact time. The measurements were performed with a pH meter connected to a glass-body combination electrode (Mettler-Toledo), which was regularly calibrated with standard buffers for pH 4, 7, and 10. The results and corresponding discussion can be found in the Supplementary Information (Section 1, Supporting Information).

Catalyst Synthesis: Typically, ammonium heptamolybdate ($(NH_4)_6Mo_7O_{24}\cdot 4H_2O$) and diammonium hydrogen phosphate ($(NH_4)_2 HPO_4$) (P/Mo = 1.5) were dissolved in deionized water (pH = 6–7) and impregnated drop-wise onto the support until incipient wetness with continuous stirring. The impregnated support was held at room temperature for 12 h before being dried at 120 °C for 2 h and calcined at 500 °C for 3 h. The promoters Ni (5 wt%), Co (3 wt%), and Pd (5 wt%) were added in the form of aqueous nitrate precursor solutions via incipient wetness impregnation, followed by the same drying and calcination procedure as described above. The calcined catalyst precursor was subjected to TPR in a H_2 flow of 120 cm^3 (standard pressure and temperature [1 atm and °C, respectively]—STP) min^{-1} g_{cat}^{-1}, at a temperature ramp of 1 °C min^{-1} to a final temperature of 700 °C. The final temperature was held for 1 h. Then, the catalyst was cooled to room temperature in Ar, and prior to removal from the reactor, the catalyst was passivated in 2 vol% O_2 in Ar for 2 h at room temperature. Preparation of the K-promoted catalysts was achieved by first impregnating the support with a solution of potassium nitrate (KNO_3) containing the required amount of KNO_3 dissolved in de-ionized water for incipient wetness impregnation. After aging at room temperature for 12 h, the impregnated support was dried at 120 °C for 2 h followed by calcination at 500 °C for 3 h. Subsequently, the K-support was impregnated with $(NH_4)_6Mo_7O_{24}$ $4H_2O$ and $(NH_4)_2HPO_4$, dried, calcined, and subjected to TPR as before. In the present study, catalysts are denoted as (*x*)-KMoP/support (*y*), where *x* is the K/Mo molar ratio and *y* is specified as the P/Mo molar ratio, weight loading of Mo, or weight loading of K.

MC (Starbon 800) was impregnated with the precursor solutions as described above. The calcination step described for the silica-supported catalysts was replaced with an annealing step under a N_2 atmosphere at 500 °C for 4 h.

Catalyst Characterization: X-ray Diffraction: Powder XRD patterns of the catalysts were recorded on a Phillips PANanalytical X'Pert Pro diffractometer with Cu Kα radiation ($\lambda = 1.542$ Å) and operated at 45 kV and 40 mA. High-resolution symmetric scans were conducted, with 0.01° per step and 75 s per step.

The width of a diffraction peak can be related to the average crystallite size (*d*) via the Scherrer Equation (1):

$$d = \frac{K \cdot \lambda}{\beta \cdot \cos\theta} \tag{1}$$

where *K* is the shape factor, λ is the X-ray wavelength, β is the full-width at half-maximum of a diffraction peak, and θ is the scattering angle of the considered Bragg reflection. Alternatively, the peak width can be expressed as the integral width, which is the area under the diffraction peak divided by the peak maximum. For all catalysts, the X-ray reflection at 43.0° 2θ (MoP (101)) was used to calculate the average crystallite size.

TEM: TEM was performed on an FEI Tecnai G2 F20 X-TWIN operated at a 200 kV accelerating voltage. Elemental analysis was performed on catalysts using EDS analysis, performed within the FEI Tecnai using an installed energy dispersive X-ray analysis (EDAX) EDS system with a silicon drift detector (SSD). TEM samples were prepared in air by suspending powder catalyst particles in isopropanol, sonicating for 5 min, and drop-casting them onto holey carbon-coated gold grids. Particle size histograms were derived from the images with at least 80 particles counted per sample.

X-Ray Photoelectron Spectroscopy: The oxidation states were studied using XPS (PHI 5000 VersaProbe) with Al Kα 1486.6 eV radiation. All spectra were calibrated to the line position of adventitious carbon at 284.8 eV.

X-Ray Absorption Spectroscopy and NEXAFS Spectroscopy: Mo K-edge (20 000 eV) X-ray absorption spectra were collected on beamline 9-3 at the Stanford Synchrotron Radiation Lightsource (SSRL). The spectra of ex situ-activated and post-catalysis samples were acquired in the transmission mode using self-supporting pellets of the powder materials at room temperature averaging three scan sweeps.

P K-edge NEXAFS data were collected on beamline 14-3 at SSRL in the fluorescence mode. Air-exposed samples were diluted to 1 wt% P in boron nitride to avoid significant self-absorption phenomena, and data were collected in the fluorescence mode using a four-element SSD (Vortex) inside a He-filled chamber to avoid X-ray attenuation by air. At least four scan sweeps were averaged together before data normalization. Data were analyzed using the Demeter software package.[58] After averaging several scan sweeps, a linear pre-edge was subtracted, and the data were normalized by the edge jump. A background, approximated with a spline function, was subtracted from the data to isolate $\chi(k)$ that was k^3-weighted prior to FT. The coordination numbers (*N*), the distance to the scattering atoms (*R*), and the mean-squared displacement (σ^2) were obtained by nonlinear fitting with least-squares refinement to the EXAFS equation of the FT data in q-space.

X-ray Fluorescence: XRF was performed on a Spectro Xepos HE XRF Spectrometer. A total of 0.1–0.3 g of catalyst powder was loaded for each measurement. Calculations were made using the instrument's "TQ powders" setting, based on first principles.

Catalytic Testing: All catalysts were tested in a high-pressure stainless steel flow reactor. A gas purifier (Pall Gaskleen ST) containing zeolite and sodium was used in CO hydrogenation experiments to remove carbonyl species as well as any trace oxygen and moisture contaminants upstream of the reactor. Products were analyzed using an Agilent gas chromatography-mass spectrometry (GC-MS) equipped with mass spectrometer, flame ionization, and thermal conductivity detectors and DB-624, DB 1, PLOT Q, HayeSepQ, and Shin Carbon columns. Typically, 200–250 mg of catalyst was used in sieve fractions of 150–300 μm. Catalysts were reduced in situ at 400 °C in flowing hydrogen for 1 h prior to each test. Catalysts were tested for CO hydrogenation activity at 230–270 °C, 3–6 MPa, and $H_2/CO = 1–3$. The gas flow was adjusted to the catalyst bed height so that the gas hourly space velocities (GHSVs) were fixed at $\approx$2600 h^{-1} for all catalysts. Argon was used as an internal standard to calculate the molar flow rates of product species. All selectivity values reported in this work are weighted by the carbon number of the product species. For some experiments, the temperature was increased stepwise with 10 °C per step to 300 °C to calculate the activation energies (see Section 4.6.2).

Kinetic Studies: Product Distribution : ASF plots for the distribution of alcohol and hydrocarbon products were constructed with catalytic data obtained after 35 h of reaction. The chain growth probability (α) was calculated with Equation (2).[59] W_n is the mass fraction of the species with carbon number n. When $\ln(W_n/n)$ is plotted against the carbon number, the slope of the trendline yields the value for α.

$$\ln(W_n/n) = n \cdot \ln(\alpha) + \text{constant} \tag{2}$$

Activation Energies: Arrhenius Equation (3) was used to calculate the activation energies for CO conversion and different products. This equation relates the rate of a reaction, in this case the CO conversion rate or the formation rate of a specific product, with the temperature (energy) of the system. The Arrhenius factor (A) is a constant related to the geometry needed, r is the reaction rate, R is the gas constant (8.314 J · mol^{-11} K^{-1}), T is the temperature in Kelvin. P^{α}_{CO} and $P^{\beta}_{H_2}$ are, respectively, the partial pressures in the reactants CO, with reaction order α, and H_2, with reaction order β. These are kept constant during experiments to determine the activation energies. Rearranging and taking the natural logarithm of this equation yielded a "straight-line" format (4), where $\ln(A)$, $\ln(P^{\alpha}_{CO})$, and $\ln(P^{\beta}_{H_2})$ are constants. When $\ln(r)$ vs the inverse of the temperature was plotted, the slope was a straight line. The value of the slope was equal to $-E_a/R$.

$$r = A \cdot e^{-E_a/RT} \cdot P^{\alpha}_{CO} \cdot P^{\beta}_{H_2} \tag{3}$$

$$\ln(r) = -\frac{E_a}{R} \cdot \left[\frac{1}{T}\right] + \ln(A) + \ln(P^{\alpha}_{CO}) + \ln(P^{\beta}_{H_2}) \tag{4}$$

Supporting Information

Supporting Information is available from the Wiley Online Library or from the author.

Acknowledgements

I.C.t.H. and E.V. contributed equally to this work. The US Department of Energy (DOE) Office of Basic Energy Sciences (BES) is gratefully acknowledged for primary support for the SUNCAT Center for Interface Science and Catalysis. This work was supported by the Global Climate & Energy Project (GCEP) at Stanford University. Additional support for aspects of this work (elucidation of structure-activity relationships using advanced characterization techniques) was provided by the US Department of Energy, Chemical Sciences, Geosciences, and Biosciences (CSGB) Division of the Office of Basic Energy Sciences, via Grant DE-AC02-76SF00515 to the SUNCAT Center for Interface Science and Catalysis. TEM, XRD, and XPS were performed at the Stanford Nano Shared Facilities (SNSF) at Stanford University, supported by the National Science Foundation under award ECCS-1542152. Use of the Stanford Synchrotron Radiation Lightsource (SSRL), SLAC National Accelerator Laboratory, is supported by the US Department of Energy, Office of Basic Energy Sciences under Contract No. DE-AC02-76SF00515. Technical support from SSRL staff, Matthew Latimer, and Erik Nelson during experiments at SSRL Experimental Station 9-3 and 14-3 is greatly appreciated. The authors gratefully acknowledge Andrew Riscoe for the nitrogen physisorption measurements.

Conflict of Interest

The authors declare no conflict of interest.

Keywords

higher alcohol synthesis, molybdenum phosphide, promoter effects, support effects, syngas conversion

Received: December 2, 2018
Revised: February 4, 2019
Published online: April 12, 2019

[1] R. G. Herman, *Catal. Today* **2000**, *55*, 233.
[2] J. J. Spivey, A. Egbebi, *Chem. Soc. Rev.* **2007**, *36*, 1514.
[3] S. Zaman, K. J. Smith, *Catal. Rev.* **2012**, *54*, 41.
[4] H. T. Luk, C. Mondelli, C. Ferre, J. A. Stewart, J. Pe, *Chem. Soc. Rev.* **2016**, *46*, 1358.
[5] X. Kang, B. A. O. Zhenghong, Q. I. Xingzhen, W. Xinxing, Z. Liangshu, *Chinese J. Catal.* **2013**, *34*, 116.
[6] K. Klier, *Adv. Catal.* **1982**, *31*, 243.
[7] R. A. van Santen, A. J. Markvoort, I. A. W. Filot, M. M. Ghouri, E. J. M. Hensen, *Phys. Chem. Chem. Phys.* **2013**, *15*, 17038.
[8] A. J. Medford, A. C. Lausche, B. Temel, N. C. Schjødt, J. K. Nørskov, F. Studt, *Top. Catal.* **2014**, *57*, 135.
[9] N. Yang, J. S. Yoo, J. Schumann, P. Bothra, J. A. Singh, E. Valle, F. Abild-Pedersen, J. K. Nørskov, S. F. Bent, *ACS Catal.* **2017**, *7*, 5746.
[10] M. Xiang, D. Li, W. Li, B. Zhong, Y. Sun, *Catal. Commun.* **2007**, *8*, 513.
[11] S. F. Zaman, K. J. Smith, *Catal. Commun.* **2009**, *10*, 468.
[12] C. H. Ma, H. Y. Li, G. D. Lin, H. B. Zhang, *Catal. Lett.* **2010**, *137*, 171.
[13] C. H. Ma, H. Y. Li, G. D. Lin, H. B. Zhang, *Appl. Catal., B* **2010**, *100*, 245.
[14] S. F. Zaman, K. J. Smith, *Appl. Catal., A* **2010**, *378*, 59.
[15] J.-J. Wang, J.-R. Xie, Y.-H. Huang, B.-H. Chen, G.-D. Lin, H.-B. Zhang, *Appl. Catal., A* **2013**, *468*, 44.
[16] P. E. Boahene, V. R. Surisetty, R. Sammynaiken, A. K. Dalai, *Top. Catal.* **2014**, *57*, 538.
[17] T. Toyoda, T. Minami, E. W. Qian, *Energy Fuels* **2013**, *27*, 3769.
[18] M. Konarova, F. Tang, J. Chen, G. Wang, V. Rudolph, J. Beltramini, *ChemCatChem* **2014**, *6*, 2394.
[19] Y. Liu, K. Murata, M. Inaba, *React. Kinet., Mech. Catal.* **2014**, *113*, 187.
[20] S. T. Oyama, *J. Catal.* **2003**, *216*, 343.
[21] M. Xiang, D. Li, H. Xiao, J. Zhang, H. Qi, W. Li, B. Zhong, Y. Sun, *Fuel* **2008**, *87*, 599.
[22] S. F. Zaman, N. Pasupulety, A. A. Al-Zahrani, M. A. Daous, S. S. Al-Shahrani, H. Driss, L. A. Petrov, K. J. Smith, *Appl. Catal., A* **2017**, *532*, 133.
[23] V. P. Santos, B. Van Der Linden, A. Chojecki, G. Budroni, S. Corthals, H. Shibata, G. R. Meima, F. Kapteijn, M. Makkee, J. Gascon, *ACS Catal.* **2013**, *3*, 1634.
[24] J. M. Christensen, P. M. Mortensen, R. Trane, P. A. Jensen, A. D. Jensen, *Appl. Catal., A* **2009**, *366*, 29.
[25] M. Duyar, C. Tsai, J. L. Snider, J. A. Singh, A. Gallo, J. S. Yoo, A. J. Medford, F. Abild-Pedersen, F. Studt, J. Kibsgaard, S. Bent, J. K. Nørskov, T. Jaramillo, *Angew. Chem., Int. Ed.* **2018**, *57*, 15045
[26] P. A. Clark, S. T. Oyama, *J. Catal.* **2003**, *218*, 78.
[27] Y. Shu, S. T. Oyama, *Carbon* **2005**, *43*, 1517.
[28] C. T. Campbell, *Science* **2002**, *298*, 811.
[29] X. M. Ma, G. D. Lin, H. B. Zhang, *Catal. Lett.* **2006**, *111*, 141.
[30] S. F. Zaman, K. J. Smith, *Catal. Today* **2011**, *171*, 266.
[31] R. Andersson, M. Boutonnet, S. Järs, *Appl. Catal., A* **2012**, *417–418*, 119.
[32] Z. Fan, W. Chen, X. Pan, X. Bao, *Catal. Today* **2009**, *147*, 86.
[33] S. H. Chai, J. Y. Howe, X. Wang, M. Kidder, V. Schwartz, M. L. Golden, S. H. Overbury, S. Dai, D. E. Jiang, *Carbon* **2012**, *50*, 1574.

[34] S. H. Chai, V. Schwartz, J. Y. Howe, X. Wang, M. Kidder, S. H. Overbury, S. Dai, D. E. Jiang, *Microporous Mesoporous Mater.* **2013**, *170*, 141.
[35] D. Ferrari, G. Budroni, L. Bisson, N. J. Rane, B. D. Dickie, J. H. Kang, S. J. Rozeveld, *Appl. Catal., A* **2013**, *462–463*, 302.
[36] N. Kumar, M. L. Smith, J. J. Spivey, *J. Catal.* **2012**, *289*, 218.
[37] J. M. Christensen, A. J. Medford, F. Studt, A. D. Jensen, *Catal. Lett.* **2014**, *144*, 777.
[38] J. Baxter, Z. Bian, G. Chen, D. Danielson, M. S. Dresselhaus, A. G. Fedorov, T. S. Fisher, C. W. Jones, E. Maginn, U. Kortshagen, A. Manthiram, A. Nozik, D. R. Rolison, T. Sands, L. Shi, D. Sholl, Y. Wu, *Energy Environ. Sci.* **2009**, *2*, 559.
[39] M. Taborga Claure, S. H. Chai, S. Dai, K. A. Unocic, F. M. Alamgir, P. K. Agrawal, C. W. Jones, *J. Catal.* **2015**, *324*, 88.
[40] X. Wang, P. Clark, S. Oyama, *J. Catal.* **2002**, *208*, 321.
[41] I. I. Abu, K. J. Smith, *J. Catal.* **2006**, *241*, 356.
[42] J. Kibsgaard, T. F. Jaramillo, *Angew. Chem., Int. Ed.* **2014**, *53*, 14433.
[43] R. Prins, M. E. Bussell, *Catal. Lett.* **2012**, *142*, 1413.
[44] J. A. Bergwerff, T. Visser, B. R. Leliveld, B. D. Rossenaar, K. P. de Jong, B. M. Weckhuysen, *J. Am. Chem. Soc.* **2004**, *126*, 14548.
[45] J. Bai, X. Li, A. Wang, R. Prins, Y. Wang, *J. Catal.* **2013**, *300*, 197.
[46] J. G. Nunan, C. E. Bogdan, K. Klier, K. J. Smith, C. W. Young, R. G. Herman, *J. Catal.* **1989**, *116*, 195.
[47] A. M. Hilmen, M. Xu, M. J. Gines, E. Iglesia, *Appl. Catal., A* **1998**, *169*, 355.
[48] E. M. Calverley, K. T. Smith, *J. Catal.* **1991**, *130*, 616.
[49] S. T. Oyama, P. Clark, V. L. Teixeira da Silva, E. J. Lede, F. G. Requejo, *J. Phys. Chem. B* **2002**, *105*, 4961.
[50] A. Markowicz, D. Wegrzynek, E. Chinea-Cano, S. A. Bamford, D. H. Torres, R. P. Alvarez, *X-Ray Spectrom.* **2007**, *36*, 27.
[51] B. Wen, N. A. Chernova, R. Zhang, Q. Wang, F. Omenya, J. Fang, M. S. Whittingham, *Chem. Mater.* **2013**, *25*, 3513.
[52] D. C. Phillips, S. J. Sawhill, R. Self, M. E. Bussell, *J. Catal.* **2002**, *207*, 266.
[53] Z. Huang, H. Hou, C. Wang, S. Li, Y. Zhang, X. Ji, *Chem. Mater.* **2017**, *29*, 7313.
[54] T. Y. Park, I.-S. Nam, Y. G. Kim, *Ind. Eng. Chem. Res.* **1997**, *36*, 5246.
[55] X. Ning, Z. An, J. He, *J. Catal.* **2016**, *340*, 236.
[56] V. S. Dorokhov, E. A. Permyakov, P. A. Nikulshin, V. V. Maximov, V. M. Kogan, *J. Catal.* **2016**, *344*, 841.
[57] L. E. Y. Nonneman, A. G. T. M. Bastein, V. Ponec, R. Burch, *Appl. Catal.* **1990**, *62*, 23.
[58] B. Ravel, M. Newville, *J. Synchrotron Radiat.* **2005**, *12*, 537.
[59] M. Claeys, E. van Steen, in *Studies in Surface Science and Catalysis* (Eds: A. Steynberg, M. Dry), Vol. *152*, Elsevier **2004**, pp. 601–680, Ch. 8.